Near Surface Properties of Martian Regolith Derived From InSight HP 3 -RAD Temperature Observations During Phobos Transits

N. Mueller, S. Piqueux, M. Lemmon, J. Maki, R. D Lorenz, M. Grott, T. Spohn, S. E Smrekar, J. Knollenberg, T. L Hudson, et al.

Geophysical Research Letters

RESEARCH LETTER
10.1029/2021GL093542

Key Points:

- The Martian surface temperature response to Phobos transits at the InSight landing site is interpreted
- The thermal inertia of the uppermost layer of soil is $103^{+22}_{-16}\,\mathrm{Jm^{-2}K^{-1}s^{-1/2}}$
- The thermal conductivity or density of the top 0.2–4 mm is significantly less than that of the top 4 cm

Supporting Information:

Supporting Information may be found in the online version of this article.

Correspondence to:

N. Mueller,
nils.mueller@dlr.de

Citation:

Mueller, N., Piqueux, S., Lemmon, M., Maki, J., Lorenz, R. D., Grott, M., et al. (2021). Near surface properties of Martian regolith derived from InSight HP^3-RAD temperature observations during Phobos transits. *Geophysical Research Letters*, *48*, e2021GL093542. https://doi.org/10.1029/2021GL093542

Received 2 APR 2021
Accepted 16 JUL 2021

Near Surface Properties of Martian Regolith Derived From InSight HP^3-RAD Temperature Observations During Phobos Transits

N. Mueller[1], S. Piqueux[2], M. Lemmon[3], J. Maki[2], R. D. Lorenz[4], M. Grott[1], T. Spohn[1,5], S. E. Smrekar[2], J. Knollenberg[1], T. L. Hudson[2], C. Krause[6], E. Millour[7], F. Forget[7], M. Golombek[2], A. Hagermann[8], N. Attree[9], M. Siegler[10], and W. B. Banerdt[2]

[1]German Aerospace Center (DLR), Institute of Planetary Research, Berlin, Germany, [2]Jet Propulsion Laboratory, California Institute of Technology, Pasadena, CA, USA, [3]Space Science Institute, College Station, TX, USA, [4]Johns Hopkins Applied Physics Laboratory, Laurel, MD, USA, [5]International Space Science Institute, Bern, Switzerland, [6]Microgravity User Support Center, German Aerospace Center (DLR), Cologne, Germany, [7]Laboratoire de Météorologie Dynamique (LMD/IPSL), Sorbonne Université, Centre National de la Recherche Scientifique, École Polytechnique, École Normale Supérieure, Paris, France, [8]Luleå University of Technology, Space Campus, Kiruna, Sweden, [9]Faculty of Natural Sciences, University of Stirling, Stirling, UK, [10]PSI, SMU Earth Science, Dallas, TX, USA

Abstract We use the Martian surface temperature response to Phobos transits observed next to the InSight lander in Elysium Planitia to constrain the thermal properties of the uppermost layer of regolith. Modeled transit lightcurves validated by solar panel current measurements are used to modify the boundary conditions of a 1D heat conduction model. We test several model parameter sets, varying the thickness and thermal conductivity of the top layer to explore the range of parameters that match the observed temperature response within its uncertainty both during the eclipse as well as the full diurnal cycle. The measurements indicate a thermal inertia (TI) of 103^{+22}_{-16} $\mathrm{Jm^{-2}K^{-1}s^{-1/2}}$ in the uppermost layer of 0.2–4 mm, significantly smaller than the TI of $200\mathrm{Jm^{-2}K^{-1}s^{-1/2}}$ derived from the diurnal temperature curve. This could be explained by larger particles, higher density, or some or slightly higher amount of cementation in the lower layers.

Plain Language Summary The Mars moon Phobos passed in front of the Sun from the perspective of the InSight lander on several occasions. The Mars surface temperatures measured by the lander became slightly colder during these transits due to the lower amount of sunlight the surface received at this time. The transits only last 20–35 s and therefore only the very top layer, about 0.3–0.8 mm, of the ground has time to cool significantly. The top layer cools and heats up faster than we expected based on the temperature changes of the day-night cycle, which affects about 4 cm of the ground. Based on this observation we conclude that the material in the top mm of the ground is different from that below. A possible explanation would be an increase of density with depth, a larger fraction of smaller particles such as dust at the top, or a layer where particles are slightly cemented together beginning at 0.2–4 mm below the surface.

1. Introduction

Observations of the brightness temperature in response to changes in insolation constrain the thermophysical properties of the upper layer of planetary surfaces, most frequently reported as thermal inertia (TI) defined as the root of the product of volumetric heat capacity ρc and thermal conductivity k. The thermal conductivity constrains the particle size of the regolith (Presley & Christensen, 1997a, 1997b, 1997c; Piqueux & Christensen, 2009a) but is also highly sensitive to cementation (Piqueux & Christensen, 2009b). The depth of regolith that can be probed is approximately the diurnal skin depth $d = \sqrt{kD\,/\,(\pi\rho c)}$, where D is the duration of the Martian day. The skin depth is ~4 cm when adopting the volumetric heat capacity $\rho c = 8.2 \cdot 10^5 \mathrm{JK^{-1}m^{-3}}$ from Morgan et al. (2018) and thermal conductivity k according to the orbiter derived TI of the InSight landing site of 200 $\mathrm{Jm^{-1}K^{-1}s^{-1/2}}$ (Golombek, Warner, et al., 2020). If the diurnal temperature curve of the same location is sampled at sufficiently separate local times, typically using in-situ observations (Fergason et al., 2006; Hamilton et al., 2014) instead of sun-synchronous orbiters, it is also

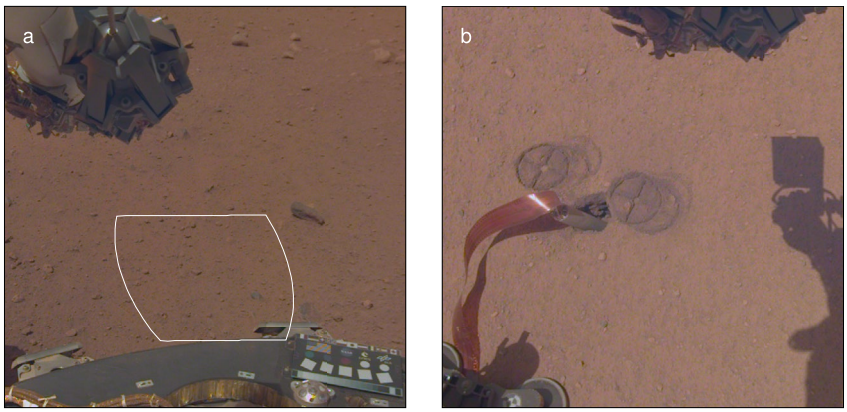

Figure 1. Panel (a) outlines the area observed by the radiometer used in this study in a portion of image D001L0010_597418893CPG_F0004C0010M2. The area is 3–4 m North-North-West of the lander center. Panel (b) shows the situation of the HP^3 mole on sol 230 (D006L0230_616943645CPG_F0505_0080M8), after the support structure initially holding the mole has been removed. The hole created by the penetration attempts indicates that the regolith has sufficient strength to support vertical or even overhanging walls, possibly with clasts embedded. The mole is 2 m SSE of the lander center (Golombek, Williams, et al., 2020).

possibly to infer layering within the diurnal skin depth (Edwards et al., 2018; Piqueux et al., 2021; Vasavada et al., 2017).

Golombek et al. (2017) state that the TI of the InSight landing ellipse derived from orbit (200 $Jm^{-1}K^{-1}s^{-1/2}$) is "consistent with a surface composed of cohesionless sand size particles or a mixture of slightly cohesive soils (cohesions of less than a few kPa)" covered by a coating of surface dust responsible for the high albedo of 0.24, which is too thin to affect the diurnal curve. The TI map created by Golombek et al. (2017) using 100 m spatial scale Thermal Imaging System data (Christensen et al., 2004) indicates a TI of 166 $Jm^{-1}K^{-1}s^{-1/2}$ in the immediate surroundings of the lander (Golombek, Kass, et al., 2020), consistent with the TI of $183\pm25 Jm^{-1}K^{-1}s^{-1/2}$ derived from HP^3 RAD diurnal temperatures by Piqueux et al. (2021). Thus there is no evidence for unexpected properties of the regolith at the landing site; however, the Heat Flow and Physical Properties Package (HP^3) mole (Spohn et al., 2018) failed to deploy its instrumented tether to the subsurface (Figure 1). The mole is designed to measure thermal conductivity and the results at its current position in the top 40 cm of regolith are consistent with the observed TI (Grott et al., 2021; Piqueux et al., 2021). The steep wall of the pit created by the penetration attempt, and clasts embedded therein, have been interpreted as evidence for a duricrust (Golombek, Warner, et al., 2020), that is, that the bonds between grains are strengthened by a cementing material. This raises the question of whether the particles are smaller than thought, since such cementation has the potential to strongly increase the thermal conductivity (Piqueux & Christensen, 2009b).

Transits of the Martian moons, which eclipse a significant fraction of the Sun's disc, provide a shorter stimulus than the diurnal cycle. Phobos transits, with a typical duration of 20–30 s, have a skin depth d of 0.3–0.8 mm, assuming a thermal conductivity of 0.01–0.05 $Wm^{-1}K^{-1}$ corresponding to dust and fine sands, respectively (Presley & Christensen, 1997b). The change in temperature in response to a Phobos transit has been observed by the Thermoskan instrument on the 1989 Phobos 2 mission (Betts et al., 1995). The THEMIS instrument on the Mars Odyssey orbiter observed the Phobos shadow but could not resolve the temperature response (Piqueux & Christensen, 2012). At the InSight landing site, the effect of several Phobos transits was observed with different geophysical instruments (Stähler et al., 2020) including the SEIS Very Broad Band seismometer and the infrared radiometer (RAD) of the HP^3 instrument (Mueller et al., 2020; Spohn et al., 2018). RAD is mounted under the lander deck and has two unobstructed 20° fields of view of two spots in 1.5 and 3.5 m distance North-North-West from the lander center. The lander has a significant effect on the closer spot and we limit this study to the farther spot, which is not significantly affected. An outline of the footprint is shown superposed in Figure 1a The spectral channel used in this study has a wavelength bandpass from 8 to 14 μm. Surface temperature has been derived from the infrared flux in this band using Planck's law and an emissivity of 0.98 (Morgan et al., 2018).

Table 1
The Observed Transits Differ in Solar Elevation e_{sol}, Duration t_{ecl}, Visible Wavelength Dust Opacity τ, Observed Temperature Difference Between Start and Minimum During the Transit ΔT_{min}, Assumed Error of Temperature Observation σT_{obs}, Temperature Equivalent of the Assumed Error in Flux Variation due to Phobos Position Uncertainty σT_{pos}, Which Results in Variations of the Fitted Thermal Conductivity of the Top Layer k_1 and its Uncertainty

Sol	LTST	e_{sol}[°]	t_{ecl} [s]	τ	ΔT_{min}[K]	σT_{obs}[K]	σT_{pos}[K]	$k_1[\frac{mW}{m \cdot K}]$	ΔT_{mod}[K]
96	13:06	71	24.3	1.05	1.22	0.24	0.22	19^{+27}_{-10}	−1.37
97	11:15	76	26.7	1.04	1.82	0.25	0.26	25^{+11}_{-8}	−2.22
99	15:53	31	20.1	0.94	0.41	0.11	0.08	7^{+16}_{-3}	−0.74
498	17:24	8.6	34.8	0.69	0.40	0.03	0.005	26^{+10}_{-8}	2.50
499	15:41	34	25.4	0.73	0.78	0.15	0.11	12^{+12}_{-5}	−0.54
501	12:03	82	26.3	0.70	2.33	0.24	0.29	13^{+6}_{-4}	−0.39

Note. The difference of the fitted diurnal curve to the measurements at start of the transit are provided under ΔT_{mod}.
Abbreviation: LTST, local true solar time.

InSight's rocket assisted landing has reduced the albedo locally by removal of the surficial dust layer (Golombek, Warner, et al., 2020). Though some dust might have been shielded behind topographic highs (see Figure 19 in Golombek, Kass, et al. [2020]), the reduction in albedo indicates that the remaining top material particles are coarser than the brighter aeolian dust. Based on the footprints of the HP^3 support structure and interactions with the robotic arm scoop the upper few mm are also interpreted as unconsolidated, uncemented material (Golombek, Warner, et al., 2020). Observing the temperature response to the transit in addition to the diurnal response allows us to detect a change of thermal conductivity, which is expected if there is indeed a difference in the amount of cementation between the top mm and the diurnal skin depth of a few cm.

2. Phobos Transits

HP^3-RAD acquired data at the maximum sampling rate of 1/2 Hz during six transits of the Mars moon Phobos (Table 1). To interpret the temperature response it is necessary to quantify the change in insolation during these transits. The most direct measurement of insolation variation can be obtained from recordings of the solar panel currents (Lorenz et al., 2020). During the first three transits, the solar panels acquired data only at 1/30 Hz, while later the sampling rate was increased to 1/4 Hz.

To provide light curves at sufficient time resolution to model the temperature response, we use the limb finding routine of the SPICE toolkit (Acton, 1996; Acton et al., 2018) to generate a series of simulated images of the transits (Figure 2a). The shape model of Phobos used in this step was created by Willner et al. (2014). The Phobos position is calculated using the ephemerides SPICE kernels "mar97s.bsp" together with other kernels from the InSight collection. The solar limb darkening function is taken from Neckel and Labs (1994) for the solar spectrum maximum at 550 nm. The variation of limb darkening in the visible band from 440 to 880 nm does not significantly change the results.

The aggregate brightness of all pixels of each frame is divided by the aggregate brightness of a frame where Phobos does not obscure any part of the solar disk to generate the curve of relative insolation. This is multiplied with the downwelling visible flux generated by the KRC model (Kieffer, 2013) for the appropriate season and local time, as well as the dust opacity as derived from camera observations (e.g., Banfield et al., 2020), more details about the model input parameters are in Section 3.

The position uncertainty of Phobos results in an uncertainty of the light curves. The error of closest angular separation of Sun and Phobos (and thus the amplitude of the insolation loss) is mostly determined by the position error along the normal of Phobos' orbital plane, closely aligned with its rotation axis. Recent work

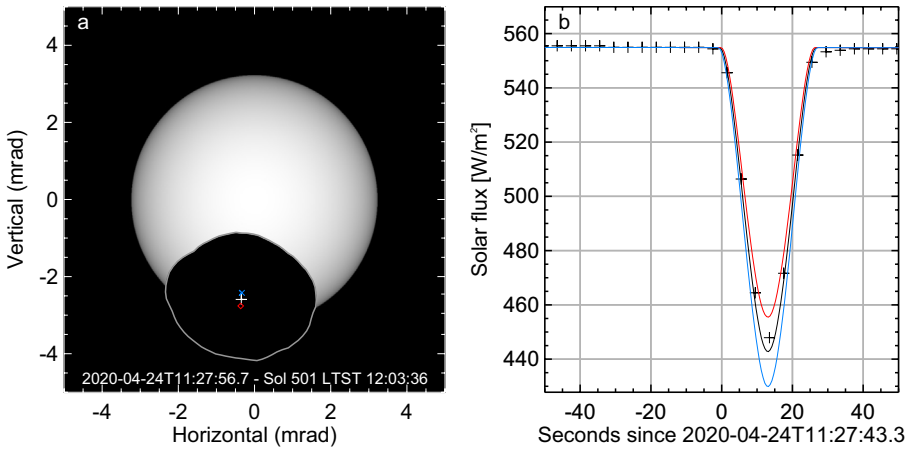

Figure 2. Panel (a) shows a simulated image of the outline of Phobos obscuring the disc of the sun at the moment of closest approach. The relative brightness is shown as grayscale. Shown as blue cross and red diamond here are offsets of 1 km along Phobos' rotation axis toward N and S, respectively. Panel (b) shows a model of the downwelling visible solar flux in comparison to scaled solar panel currents (+symbols). The blue and red light curves correspond to the offset in Phobos position outlined in panel (a) in the same colors.

by Lainey et al. (2020) shows out-of-plane position differences to the mar97 ephemerides on the order of 1 km and we adopt this value as out-of-plane error as a worst-case assumption. The change in apparent Phobos position at closest separation to the sun and the corresponding variation in the light curve is presented in Figure 2.

The solar array current is scaled with a conversion factor specific to each transit so that the scaled flux matches the modeled visible flux directly before the transit. The modeled light curves and solar panel data are shown for sol 501 in Figure 2b. The equivalent plots for all transits are shown in the supplement. Solar array data and modeled light curves fit well within the adopted uncertainty, with the exceptions of sols 99 and 498. The bad fit of these transits occurring late in the afternoon is likely a result of scattering and refraction in the atmosphere, as discussed in Stähler et al. (2020). This appears to reduce the effect of the eclipses although at solar elevations greater or equal to that of sol 499 (34°) the deviation is within the uncertainty from the position of Phobos. Table 1 provides the solar elevation angle for the different transits.

3. Transit Temperature Response

The temperatures observed by the HP^3 radiometer during the transit and the diurnal temperature curves of sol 501 are shown in Figure 3, with the corresponding plots of all transits shown in the supplement. The total uncertainty of the RAD measurements is dominated by potential calibration errors (Mueller et al., 2020), which do not change significantly over the period of the eclipse. To quantify the uncertainty on the time scale of the eclipse, we analyze the 10 min of 1/2 Hz data before each transit. The diurnal trend is removed by subtracting a linear fit to the whole 10 min. The standard deviation of the residual is adopted as observation error σT_{obs}.

We model surface temperatures using as boundary conditions the incident visible and infrared fluxes calculated with the KRC model. The input parameters for KRC are the regional average albedo of 0.24 and TI of 200Jm^{-2}K^{-1}s$^{-1/2}$ (Golombek et al., 2017), which have a greater influence on the atmosphere than the surface affected by the landing. The most consequential input variable is the visible wavelength atmospheric dust opacity τ (Table 1) derived from sky imaging (Banfield et al., 2020). The dust optical properties are the same as in the work of Piqueux et al. (2021) based on the work of Vasavada et al. (2017). The visible flux is modified with the relative transit light curves, as shown in Figure 2. An initial iteration of the model using these boundary conditions showed that the diurnal curves of the two seasons with transits cannot be well fitted with the same bulk TI. It is unlikely that there is a real variation of bulk TI of this magnitude and we instead add 9 Wm^{-2} to the IR fluxes during the second set of eclipses from sols 498 to 501 for the iteration

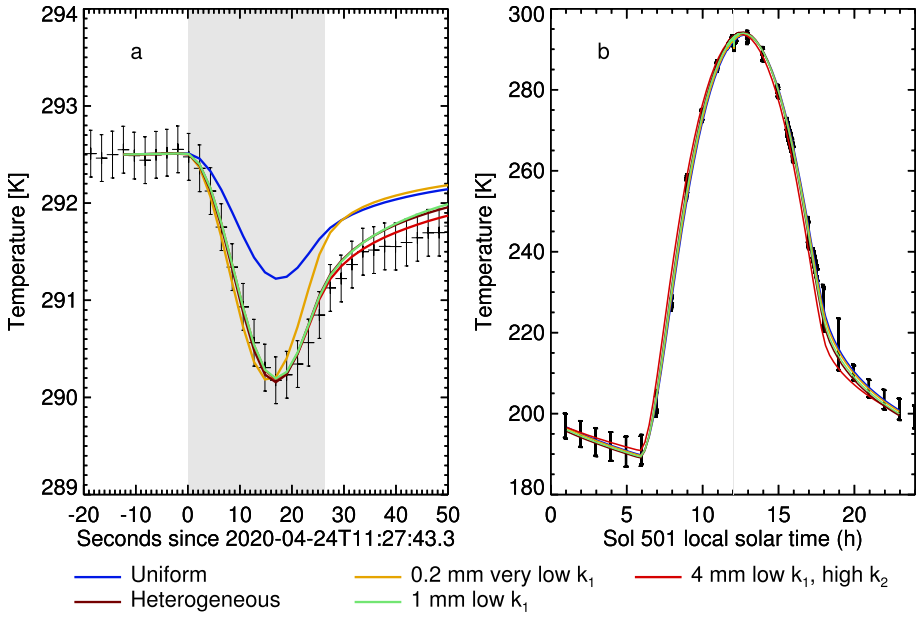

Figure 3. Measured and modeled surface temperatures near the transit on sol 501. (a) The temperature response to the transit in detail with error bars derived from the data directly before the transit as described in the text. An offset is subtracted from each model to match the data in the 20 s before the transit. (b) shows the diurnal temperature curve with error bars corresponding to the total measurement uncertainty. The different models are described in the text.

of the model presented here. This value is similar to the maximum amplitude of additional IR flux that Vasavada et al. (2017) add as a function of season to their model fitting ground temperatures observed by the radiometer on the Curiosity rover (Gómez-Elvira et al., 2012). Vasavada et al. (2017) interpret this missing flux as an effect of seasonal clouds that were not included in the model.

We solve the heat conduction equation using the implicit Euler method, which allows us to more freely vary the time and depth steps since this method is numerically unconditionally stable. The discretization scheme is based on the scheme described in the work of Kieffer (2013) and our modified equations are provided in the Supporting Information S1. The numerical layer thicknesses are 0.1 mm in the upper mm and double in thickness at each layer below that. The numerical layers are divided into two groups representing two physical layers by assigning two different values of thermal conductivity, k_1 for the top layer and k_2 for the bottom layer. The total thickness of the upper group is z_1. Time steps are 1,000 s except for the period around the eclipses, when time steps are reduced to 0.5 s. The modeled temperature response to the transit shows little sensitivity to time and depth step size as long as they are smaller than 0.5 s and 0.2 mm, respectively.

All models use a density $\rho = 1300\text{kg / m}^3$, specific heat capacity $c_p = 630\text{J / kg}$, and emissivity of 0.98 as recommended by Morgan et al. (2018). The values of thermal conductivity and heat capacity are provided for the reference temperature of 220 K and their temperature dependence in the model follows the approximations recommended by Morgan et al. (2018). The albedo is assumed to be $a = 0.16$, which both matches the estimate of a 35% darker lander blast zone than the regional average ($a = 0.24$) as well as the observed surface temperatures (Golombek, Warner, et al., 2020; Piqueux et al., 2021).

The models were adjusted by visually matching the resulting temperatures to the observations during the eclipse and over the sol of the eclipse. The aim of this manual fitting was first to generate model curves that match the amplitudes of the eclipse and diurnal response, and second to remain within the interval of uncertainty at all times.

3.1. Uniform

The subsurface is a homogeneous half-space with a thermal conductivity of 50 $\text{mW m}^{-1}\text{K}^{-1}$, corresponding to a bulk TI of 202 $\text{J m}^{-2}\text{K}^{-1}\text{s}^{-1/2}$, consistent with the value derived from the diurnal curves by Golombek, Warner, et al. (2020). This model results in a transit response too small for those sols where the insolation

dip is well understood (sols 96, 97, 499, and 501). In case of the sol 501 transit, shown in Figure 3, the model curve falls outside of the observation error bar. The model matches the diurnal temperature measurements very well (Figure 3b), indicating that the top layer causing the deeper transit response is thin compared to the diurnal skin depth of 4 cm, as discussed more detail by Piqueux et al. (2021).

3.2. 0.2 mm Very Low k_1

This model intends to represent a 0.2 mm thick top layer of fine aeolian dust with a thermal conductivity of only $k_1 = 8$ mW m^{-1}K^{-1} (TI 81 J m^{-2} K^{-1}s$^{-1/2}$). The half-space below has a thermal conductivity of 50 mW m^{-1}K^{-1}, matching the diurnal TI. This model fits the diurnal curve similarly well as the homogeneous model, and matches the amplitude of the observed temperature drop during the transit on sol 501. The shape of the transit response overall is however not a good match, the minimum occurs too early and the return to pre-transit temperatures is too fast.

3.3. 4 mm Low k_1

This model aims to represent geologic interpretations where a layer of unconsolidated regolith several mm thick (Figure 1) overlies some consolidated material with sufficient strength to support a near-vertical wall with embedded clasts (Figure 1b). The depth of the hardware footprints is at least several mm so that a thickness of 4 mm is adopted. The temperature drop of the transit on sol 501 is fitted by choosing a thermal conductivity of $k_1 = 13$ mW m^{-1}K^{-1} (TI 103 J m^{-2} K^{-1}s$^{-1/2}$). This top layer is sufficiently thick to significantly affect the diurnal temperature curve and the lower half-space thermal conductivity is increased to 80 mW m^{-1}K^{-1} (TI 255 J m^{-2} K^{-1}s$^{-1/2}$) to approximately match the observed diurnal amplitude. Increasing the top layer thickness further, or decreasing the lower half-space thermal conductivity, does not significantly affect the transit temperature minimum, and only slightly reduces the post-transit temperatures. The temperatures recorded after the transit on sol 501 (Figure 3a) seem to indicate a top layer thicker than 4 mm, but this can be ruled out by comparison to the diurnal data (see also Piqueux et al., 2021). The 4 mm top layer already cools too fast in the afternoon and evening just so that model temperatures fall outside of the total measurement error bar around 19 h local true solar time (LTST) (Figure 3b).

3.4. 1 mm Low k_1

The top layer thickness can be bounded to 0.2 mm $< z_1 <$ 4 mm by requiring the model to match the observed transit response and the diurnal curve within their respective error estimates. The best constraint is provided by the transit on sol 501 (Figure 3). For comparison of the different transits, we adopt a top layer thickness of 1 mm, which matches measurements on sol 501 well and derive the layer's thermal conductivity by matching this model to each observation. The best constraint is provided by the maximum temperature drop over the transit $\Delta T_{\min}$, which is relatively unaffected by top layer thickness or lower half-space parameters.

We assume that $\Delta T_{\min}$ can be affected by measurement errors (σT_{obs}). The models on the other hand are affected by the uncertainty in the position of Phobos, as outlined in the plot of light curves (Figure 2). For easier comparison, we express this as the temperature difference of the transit temperature minimum (σT_{pos}) calculated with the nominal model parameters and the different light curves. We add these error contributions quadratically and derive the thermal conductivities that result in the temperature drop $\Delta T_{\min}$ modified by these errors to estimate the uncertainty.

The thermal conductivities derived from the different transits are consistent with each other. The best constraint is from sol 501. The best fitting value is the same as when assuming a 4 mm layer, $k_1 = 13$ mW m^{-1} K^{-1} (TI 103 J m^{-2} K^{-1}s$^{-1/2}$). There could be a trend of decreasing thermal conductivity over time but the uncertainties are large.

3.5. Heterogeneous

We explore the possibility that pockets of low thermal conductivity material (i.e., aeolian dust) survived the landing rocket blast in topographic lows or the lee of clasts. To this end we assumed that half of the observed

surface area responds like the uniform model, and that the other half has a 1-mm thick top layer with a thermal conductivity of $k_1 = 6$ mW m^{-1}K^{-1} (TI 70 J m^{-2} K^{-1} s$^{-1/2}$), again chosen to match the temperature minimum of the transit. This model fits both the transit and diurnal curve well in all transits with high solar elevation. Clasts with diameters >20 mm cover a cumulative fractional area of of 2.5% (Golombek, Warner, et al., 2020) so that it is unlikely that the clasts themselves significantly affect the average response of the observed area.

4. Discussion and Conclusions

The transit response indicates that the thermal properties of the topmost millimeter of regolith are different from those of the underlying material within the diurnal skin depth of 4 cm. The thickness of this top layer is between 0.2 and 4 mm, bounded by the shape of the transit response and the diurnal curve, respectively. A thickness of 1 mm fits both the transit and the diurnal response well. Assuming a topmost layer thickness of 1 mm and uniform layer properties, the best constraint on top layer thermal conductivity is 13^{+6}_{-4} mW m^{-1}K^{-1}, which corresponds to a TI of 103^{+22}_{-16} J m^{-2} K^{-1} s$^{-1/2}$. At this thickness, the thermal conductivity of the lower half-space does not significantly affect the transit response.

The diurnal curves in this study can be fitted with a thermal conductivity of 50 mW m^{-1}K^{-1}, consistent with the TI of 200 ±30 J m^{-2} K^{-1} s$^{-1/2}$ from the work of Golombek, Warner, et al. (2020) and the more detailed study of the data up to sol 50 by Piqueux et al. (2021) which arrives at 183±25 J m^{-2} K^{-1} s$^{-1/2}$. The HP^3 mole, embedded in the top 37 cm of soil of a location within 6 m distance, measures a thermal conductivity of 39±2 mW m^{-1}K^{-1}, corresponding to a TI of 178±4 J m^{-2} K^{-1} s$^{-1/2}$ (Grott et al., 2021). The reason why the bulk TI appears to be changing over time is not clear yet. One possibility might be that the dust storm arriving after sol 50 (Viúdez-Moreiras et al., 2020) has changed the optical properties of the dust aerosols (Lemmon et al., 2019), which were kept constant in our modeling. The discrepancy necessitating the offset of 9 W m^{-2} in the energy budget between sols 100 and 500, equivalent to a further increase in apparent TI, could be caused by seasonally occurring clouds (Vasavada et al., 2017). We anticipate that the long-term observation of an unchanged surface location in combination with the meteorological sensors of InSight will improve our understanding of the seasonal variation of the surface energy budget, including smaller terms such as the sensible heat flux (Spiga et al., 2021). A further study of this is however beyond the scope of this paper as the main conclusion of a low TI at the surface layer is not affected by this uncertainty.

The thermal conductivity we derive for the top layer is approximately 2–4 times lower than that of the underlying material, that is, a TI contrast of approximately 1.4–2. This is similar to the results of Betts et al. (1995) who derive a TI from the Phobos transit observation that is up to two times smaller than the diurnal TI. This contrast is consistent with smaller grain size or less cementation in the top layer (Presley & Christensen, 1997c; Piqueux & Christensen, 2009b), although this is not a necessary conclusion from our observations. The most likely explanation is a combination of several plausible contributing factors: on average somewhat smaller particles due to remaining pockets of aeolian dust, densification with depth through self compaction, and potentially increasing cementation with depth.

Acknowledgments
The design, building of, and research into the HP^3 has been supported by the German Aerospace Center DLR, United States National Aeronautics and Space Administration NASA, Austrian Academy of Sciences ÖAW, and the Polish Academy of Science CBK PAN. Part of this study was performed at the Jet Propulsion Laboratory, California Institute of Technology, under a contract with NASA. US Government support acknowledged. R. D. Lorenz acknowledges NASA InSight Participating Scientist grant 80NSSC18K1626. N. Attree acknowledges support from the UK Space Agency, Grant no. ST/R001375/2.
Open access funding enabled and organized by Projekt DEAL.

Data Availability Statement

The data are archived on the Planetary Data System at https://pds-geosciences.wustl.edu/missions/insight/hp3rad.htm (The In-Sight HP3-RAD science team, 2018). This is InSight Contribution Number 138.

References

Acton, C. (1996). Ancillary data services of NASA's navigation and ancillary information facility. *Planetary and Space Science*, *44*(1), 65–70. https://doi.org/10.1016/0032-0633(95)00107-7

Acton, C., Bachman, N., Semenov, B., & Wright, E. (2018). A look towards the future in the handling of space science mission geometry. *Planetary and Space Science*, *150*, 9–12. https://doi.org/10.1016/j.pss.2017.02.013

Banfield, D., Spiga, A., Newman, C., Forget, F., Lemmon, M., Lorenz, R., et al. (2020). The atmosphere of Mars as observed by InSight. *Nature Geoscience*, *13*(3), 190–198. https://doi.org/10.1038/s41561-020-0534-0

Betts, B. H., Murray, B. C., & Svitek, T. (1995). Thermal inertias in the upper millimeters of the Martian surface derived using Phobos' shadow. *Journal of Geophysical Research*, *100*(E3), 5285–5296. https://doi.org/10.1029/95JE00226

Christensen, P. R., Jakosky, B. M., Kieffer, H. H., Malin, M. C., McSween, J., Harry, Y., et al. (2004). The thermal emission imaging system (THEMIS) for the Mars 2001 Odyssey Mission. *Space Science Reviews*, *110*(1),85–130. https://doi.org/10.1023/B:SPAC.0000021008.16305.94

Edwards, C. S., Piqueux, S., Hamilton, V. E., Fergason, R. L., Herkenhoff, K. E., Vasavada, A. R., et al. (2018). The thermophysical properties of the Bagnold Dunes, Mars: Ground-truthing orbital data. *Journal of Geophysical Research: Planets*, *123*, 1307–1326. https://doi.org/10.1029/2017JE005501

Fergason, R. L., Christensen, P. R., Bell, J. F., Golombek, M. P., Herkenhoff, K. E., & Kieffer, H. H. (2006). Physical properties of the Mars Exploration Rover landing sites as inferred from Mini-TES-derived thermal inertia. *Journal of Geophysical Research*, *111*(E2), E02S21. https://doi.org/10.1029/2005JE002583

Golombek, M., Kass, D., Williams, N., Warner, N., Daubar, I., Piqueux, S., et al. (2020). Assessment of InSight landing site predictions. *Journal of Geophysical Research: Planets*, *125*, e06502. https://doi.org/10.1029/2020JE006502

Golombek, M., Kipp, D., Warner, N., Daubar, I. J., Fergason, R., Kirk, R. L., et al. (2017). Selection of the InSight landing site. *Space Science Reviews*, *211*(1–4), 5–95. https://doi.org/10.1007/s11214-016-0321-9

Golombek, M., Warner, N. H., Grant, J. A., Hauber, E., Ansan, V., Weitz, C. M., et al. (2020). Geology of the InSight landing site on Mars. *Nature Communications*, *11*, 1014. https://doi.org/10.1038/s41467-020-14679-1

Golombek, M., Williams, N., Warner, N. H., Parker, T., Williams, M. G., Daubar, I., et al. (2020). Location and setting of the Mars InSight lander, instruments, and landing site. *Earth and Space Science*, *7*(10), e01248. https://doi.org/10.1029/2020EA001248

Gómez-Elvira, J., Armiens, C., Castañer, L., Domínguez, M., Genzer, M., Gómez, F., et al. (2012). REMS: The environmental sensor suite for the Mars science laboratory rover. *Space Science Reviews*, *170*(1–4), 583–640. https://doi.org/10.1007/s11214-012-9921-1

Grott, M., Spohn, T., Knollenberg, J., Krause, C., Hudson, T. L., Piqueux, S., et al. (2021). Thermal conductivity of the Martian soil at the InSight landing site from HP^3 active heating experiments. *Journal of Geophysical Research: Planets*, *126*, e2021JE006861. https://doi.org/10.1029/2021JE006861

Hamilton, V. E., Vasavada, A. R., Sebastián, E., Torre Juárez, M., Ramos, M., Armiens, C., et al. (2014). Observations and preliminary science results from the first 100 sols of MSL rover environmental monitoring station ground temperature sensor measurements at Gale Crater. *Journal of Geophysical Research: Planets*, *119*, 745–770. https://doi.org/10.1002/2013JE004520

Kieffer, H. H. (2013). Thermal model for analysis of Mars infrared mapping. *Journal of Geophysical Research: Planets*, *118*, 451–470. https://doi.org/10.1029/2012JE004164

Lainey, V., Pasewaldt, A., Robert, V., Rosenblatt, P., Jaumann, R., Oberst, J., & Thuillot, W. (2020). Mars moon ephemerides after 12 years of Mars express data. *Astronomy and Astrophysics*. *650*, 11. https://doi.org/10.1051/0004-6361/202039406

Lemmon, M. T., Guzewich, S. D., McConnochie, T., de Vicente-Retortillo, A., Martínez, G., Smith, M. D., et al. (2019). Large dust aerosol sizes seen during the 2018 Martian global dust event by the Curiosity Rover. *Geophysical Research Letters*, *46*, 9448–9456. https://doi.org/10.1029/2019GL084407

Lorenz, R. D., Lemmon, M. T., Maki, J., Banfield, D., Spiga, A., Charalambous, C., et al. (2020). Scientific observations with the InSight solar arrays: Dust, clouds, and eclipses on Mars. *Earth and Space Science*, *7*(5), e00992. https://doi.org/10.1029/2019EA000992

Morgan, P., Grott, M., Knapmeyer-Endrun, B., Golombek, M., Delage, P., Lognonné, P., et al. (2018). A pre-landing assessment of regolith properties at the InSight landing site. *Space Science Reviews*, *214*(6), 104. https://doi.org/10.1007/s11214-018-0537-y

Mueller, N. T., Knollenberg, J., Grott, M., Kopp, E., Walter, I., Krause, C., et al. (2020). Calibration of the HP^3 radiometer on InSight. *Earth and Space Science*, *7*(5), e01086. https://doi.org/10.1029/2020EA001086

Neckel, H., & Labs, D. (1994). Solar limb darkening 1986-1990 Lambda 303-NANOMETERS to 1099-NANOMETERS. *Solar Physics*, *153*(1–2), 91–114. https://doi.org/10.1007/BF00712494

Piqueux, S., & Christensen, P. R. (2009a). A model of thermal conductivity for planetary soils: 1. Theory for unconsolidated soils. *Journal of Geophysical Research*, *114*, E09005. https://doi.org/10.1029/2008JE003308

Piqueux, S., & Christensen, P. R. (2009b). A model of thermal conductivity for planetary soils: 2. Theory for cemented soils. *Journal of Geophysical Research*, *114*, E09006. https://doi.org/10.1029/2008JE003309

Piqueux, S., & Christensen, P. R. (2012). Visible and thermal infrared observations of the Martian surface during three Phobos shadow transits. *Geophyiscal Research Letters*, *39*, L21203. https://doi.org/10.1029/2012GL053352

Piqueux, S., Mueller, N., Grott, M., Siegler, M., Millour, E., Forget, F., & Banerdt, W. (2021). Soil thermophysical properties near the InSight lander derived from 50 sols of radiometer measurements. *Journal of Geophysical Research: Planets*, e2021JE006859. https://doi.org/10.1029/2021je006859

Presley, M. A., & Christensen, P. R. (1997a). The effect of bulk density and particle size sorting on the thermal conductivity of particulate materials under Martian atmospheric pressures. *Journal of Geophysical Research*, *102*(E4), 9221–9229. https://doi.org/10.1029/97JE00271

Presley, M. A., & Christensen, P. R. (1997b). Thermal conductivity measurements of particulate materials 1. A review. *Journal of Geophysical Research*, *102*(E3), 6535–6549. https://doi.org/10.1029/96JE03302

Presley, M. A., & Christensen, P. R. (1997c). Thermal conductivity measurements of particulate materials 2. Results. *Journal of Geophysical Research*, *102*(E3), 6551–6566. https://doi.org/10.1029/96JE03303

Spiga, A., Murdoch, N., Lorenz, R., Forget, F., Newman, C., Rodriguez, S., et al. (2021). A study of daytime convective vortices and turbulence in the Martian planetary boundary layer based on half-a-year of InSight atmospheric measurements and large-eddy simulations. *Journal of Geophysical Research: Planets*, *126*(1), e06511. https://doi.org/10.1029/2020JE006511

Spohn, T., Grott, M., Smrekar, S. E., Knollenberg, J., Hudson, T. L., Krause, C., et al. (2018). The heat flow and physical properties package (HP^3) for the InSight mission. *Space Science Reviews*, *214*(5), 96. https://doi.org/10.1007/s11214-018-0531-4

Stähler, S. C., Widmer-Schnidrig, R., Scholz, J. R., van Driel, M., Mittelholz, A., Hurst, K., et al. (2020). Geophysical observations of phobos transits by InSight. *Geophysical Research Letters*, *47*(19), e89099. https://doi.org/10.1029/2020GL089099

The InSight HP3-RAD science team. (2018). *Mars InSight Lander Radiometer Data Archive*. https://doi.org/10.17189/1517568

Vasavada, A. R., Piqueux, S., Lewis, K. W., Lemmon, M. T., & Smith, M. D. (2017). Thermophysical properties along Curiosity's traverse in Gale crater, Mars, derived from the REMS ground temperature sensor. *Icarus*, *284*, 372–386. https://doi.org/10.1016/j.icarus.2016.11.035

Viúdez-Moreiras, D., Newman, C. E., Forget, F., Lemmon, M., Banfield, D., Spiga, A., et al. (2020). Effects of a large dust storm in the near-surface atmosphere as measured by InSight in Elysium Planitia, Mars. Comparison with contemporaneous measurements by Mars science laboratory. *Journal of Geophysical Research: Planets*, *125*, e06493. https://doi.org/10.1029/2020JE006493

Willner, K., Shi, X., & Oberst, J. (2014). Phobos' shape and topography models. *Planetary and Space Science*, *102*, 51–59. https://doi.org/10.1016/j.pss.2013.12.006